Medical image synthesis using segmentation and registration

Ninon Burgos

Chapter 4

Medical image synthesis using segmentation and registration

Ninon Burgos[a,*]

[a]Sorbonne Université, Institut du Cerveau – Paris Brain Institute - ICM, CNRS, Inria, Inserm, AP-HP, Hôpital de la Pitié-Salpêtrière, F-75013, Paris, France
[*]Corresponding author: ninon.burgos@cnrs.fr

Abstract

This chapter describes how segmentation and registration can be used to synthesise medical images of a particular modality from images of another modality. Segmentation-based approaches can generally be decomposed into two components: the first one consists in segmenting the source image and the second one consists in assigning intensity values to the different tissue classes obtained to generate the desired image. The segmentation can be manual or automatic and the intensities can be assigned in bulk (i.e. with predefined values assigned to each tissue class) or in a subject-specific manner. In registration-based methods, an atlas is deformed to match the subject's anatomy using non-rigid registration. The atlas can be composed of a single image of the target modality, of a pair of images from the source and target modalities, or of multiple pairs.

Both the general principles and particular examples of segmentation-based and registration-based image synthesis approaches are described. The chapter takes as guiding thread the synthesis of computed tomography from magnetic resonance (MR) images, which is the predominant synthesis task as it answers two very concrete applications: attenuation correction of positron emission tomography (PET) data, particularly for PET/MR scanners, and radiotherapy treatment planning from MRI only.

Keywords: Image synthesis, Segmentation, Registration, Atlas database

N. Burgos and D. Svoboda (Eds.), *Biomedical Image Synthesis and Simulation*, Elsevier
https://doi.org/10.1016/B978-0-12-824349-7.00011-6

1. Introduction

Many of the early works on medical image synthesis had for objective to improve subsequent image processing steps such as segmentation or registration. In 2005, van de Kraats et al. [1] presented a new method to register (preoperative) magnetic resonance (MR) images to (intraoperative) X-ray images. MR to X-ray registration is very challenging because of the different underlying contrast mechanisms. A consequence of these differences is that several tissues, especially bone, have dissimilar appearances on both modalities, which makes it difficult to directly apply gradient-based or intensity-based registration methods. Their idea was thus to convert multispectral MR images into computed tomography (CT) images by constructing a look-up table, and to then register the synthetic CT to the X-ray, which is an easier task as both modalities have the same underlying contrast mechanisms. They showed that registering synthetic CTs to X-ray data using a gradient-based approach outperformed direct registration from the MR data. Five years later, Roy et al. [2] investigated whether lesions could be detected in the absence of an appropriate lesion-distinguishing MR sequence (a FLAIR) by synthesising a FLAIR from other sequences (T1-weighted and T2-weighted) using a patch-based approach (see Chapter 5), and showed that it was indeed the case. Other examples are described in Chapter 10.

In both these examples, image synthesis was used to improve segmentation or registration. Instead, what will be described in this chapter is how segmentation and registration can be used to synthesise medical images of a particular modality from images of another modality. The use case throughout the chapter will be the synthesis of CT from MR images as almost all the works reported target two very concrete applications: attenuation correction of positron emission tomography (PET) data, particularly for PET/MR scanners, and radiotherapy treatment planning from MRI only (more details are provided in Chapters 19 and 20.

One of the factors limiting the widespread use of PET/MR scanners is probably the imperfect attenuation correction, leading to a bias of the PET activity, particularly in the brain. Before the emergence of PET/CT scanners, attenuation correction was mostly based on transmission measurements. However, because of the restricted space and the strong magnetic field, installing a rotating radiation source in a PET/MR scanner is challenging. With PET/CT systems, the attenuation coefficients are derived from CT scans. However, in contrast with CT images, MR image intensities do not directly provide information about the tissue attenuation properties.

The aim of radiotherapy treatment planning (RTP) is to optimise the therapeutic ratio by delivering an optimal dose of radiation over the tumorous area while sparing the normal tissues. RTP first requires contouring the tumour

and organs at risk. Once these volumes have been defined, the attenuation properties of the different tissues are used as parameters in an optimisation process calculating the optimal dose distribution to treat the tumour. Most radiotherapy treatments are planned using a CT scan of the patient as its acquisition is fast and tissue attenuation coefficients can easily be derived from the CT intensity values in Hounsfield unit. However, CT images have a low soft-tissue contrast, which can lead to large organ delineation errors, particularly when located in the brain, head & neck, or pelvic regions. MRI is often preferred over CT as a structural imaging modality, mainly for its excellent soft-tissue contrast. Although MRI is increasingly used in clinical practice, its role in RTP is limited by the fact that it does not readily provide tissue attenuation properties, hampering the calculation of dose distributions. This is a critical limitation for the clinical deployment of the MR-linac devices combining an MR scanner and a linear accelerator—the machine delivering the radiation dose.

To answer these two problems, numerous methods have been proposed. Both the general principles and particular examples of segmentation-based and registration-based image synthesis approaches will be described. The reasons why these two families of methods have almost exclusively been applied to the MR to CT synthesis task and why they have been supplanted by other methods will then be discussed.

2. Segmentation-based image synthesis

Segmentation-based approaches can generally be decomposed into two components: the first one consists in segmenting the source image and the second one consists in assigning intensity values to the different tissue classes obtained to generate the desired image. The segmentation can be manual or automatic, and the intensities can be assigned in bulk (i.e. predefined values are assigned to each tissue class) or in a subject-specific manner. This process is illustrated in Figure 1. Note that segmentation-based image synthesis can also be called classification-based image synthesis [3].

2.1 Segmentation approaches

2.1.1. Manual segmentation

Manual segmentation is not uncommon in domains such as RTP [4, 5, 6]. In their early work on the use of MRI for RTP, Jonsson et al. [4] manually segmented the patient outline, bones, lungs and air cavities. An example of a pelvis MRI and synthetic CT, overlaid with patient outline and bone contours, is shown in Figure 2. Body and bone outlines were also contoured in [5] and

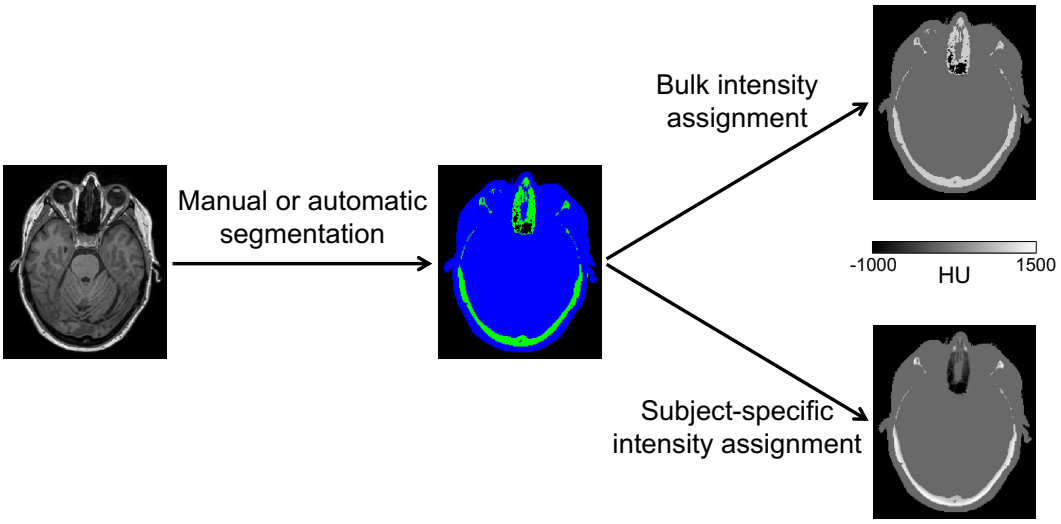

Figure 1: Segmentation-based approaches can be decomposed into two parts: the first one consists in segmenting, manually or automatically, the source image (here an MR image) and the second one consists in assigning intensity values to the different tissue classes obtained to generate the target image (here a CT image in Hounsfield unit [HU]). Intensities can be assigned in bulk (i.e. predefined values assigned to each tissue class) or in a subject-specific manner.

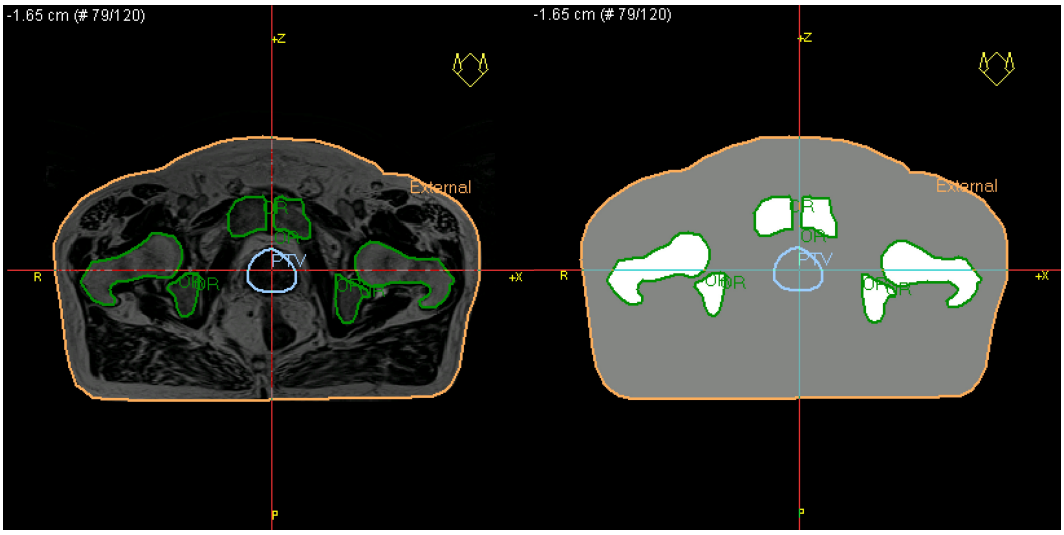

Figure 2: Example of a manually segmented MR image (left) and the resulting synthetic CT with assigned mass densities (right) [4]. *Jonsson et al. 2010 Radiat. Oncol. 5 62 doi:10.1186/1748-717X-5-62 © 2010, Jonsson et al; licensee BioMed Central Ltd.*

bone and air in [6]. Manual segmentation is very time-consuming and thus automatic segmentation methods have naturally been employed.

2.1.2. Automatic segmentation

Segmenting MR images for PET attenuation correction was already a topic of interest in the 1990s: Le Goff et al. [7] segmented brain T1-weighted (T1w) MR images based on thresholding and mathematical morphology tools. Later, Martínez-Möller et al. [8] used thresholding to segment the body into four classes: background, lungs, fat and soft-tissues. They relied on a specific MRI sequence, the Dixon method, which exploits the fact that water and fat protons have slightly different resonance frequencies. By acquiring images when their spins are in- and out-of-phase with each other, water and fat images can be derived [9]. In this work [8], a threshold was applied to the water and fat images to separate soft-tissue and fat from the background. Connected-component analysis of the air in the inner part of the body was used to define the lung class. The tissue/air classification was refined using a morphologic closing filter. Catana et al. [10] and Keereman et al. [11] also used a particular MRI sequence to segment head images into three classes (bone, soft-tissue and air), the ultra-short echo time (UTE) sequence. Two images, UTE_1 and UTE_2, were acquired at different echo times, TE_1 and TE_2 respectively, such that the bone signal is present in UTE_1 but not in UTE_2, while the signals from other tissues are similar in both images. In [10], a head mask is first obtained by applying a morphologic closing operation to the UTE_2 image. Bone tissue was segmented from a combination of the two UTE images $\left(\frac{\mathrm{UTE}_1-\mathrm{UTE}_2}{{\mathrm{UTE}_2}^2}\right)$ using an empirically determined threshold. The air cavities were segmented in the same way but from another combination of the UTE images $\left(\frac{\mathrm{UTE}_1+\mathrm{UTE}_2}{{\mathrm{UTE}_1}^2}\right)$. Finally, the voxels included in the head mask that were not identified as bone or air were classified as soft-tissue. From the two UTE images, in [11] the R2* value, which is the inverse of the T2* relaxation time, was first calculated for each voxel as follows: $\mathrm{R2^*} = \frac{\ln \mathrm{UTE}_1 - \ln \mathrm{UTE}_2}{\mathrm{TE}_2-\mathrm{TE}_1}$. It was then possible to distinguish between cortical bone, which is expected to have high R2* values, from soft-tissue, expected to have low R2* values. The distinction between air and tissue is however more difficult because of possible artefacts or noise in the UTE images. To overcome this problem, a binary air mask was created from the first-echo image (UTE_1) and applied to the R2* map. Finally, the corrected R2* map was segmented into three tissue classes (bone, soft-tissue and air) using thresholds. The method is illustrated in Figure 3. Refinements for the R2* map segmentation were later proposed [12]. Combining cortical bone segmentation and water-fat decomposition, Berker et al. [13] proposed a 4-class (bone, soft-tissue, fat and air) segmentation technique using a UTE triple-echo sequence. The combination of the first and third echoes, both in-phase, was used to segment cortical bone, while the combination of the second echo, out-of-phase, with the in-phase echoes enabled the separation of the fat and water signals and the calculation of the water-fat fraction. Bone was then segmented

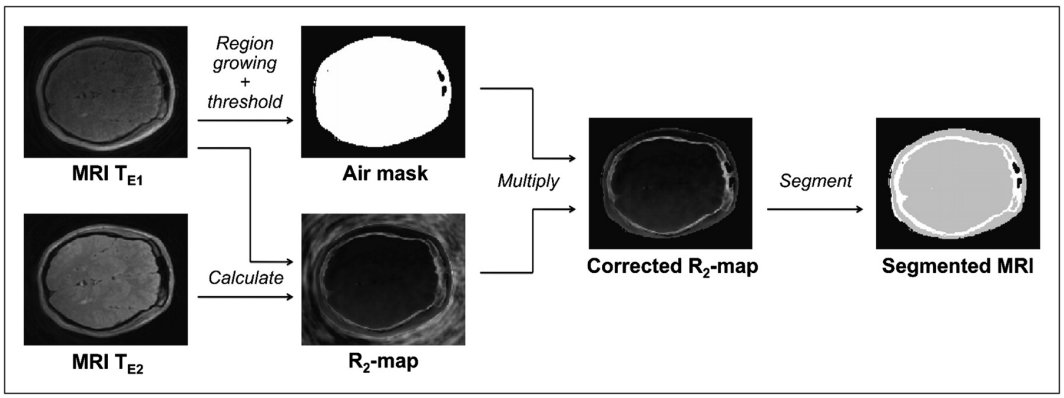

Figure 3: Automatic segmentation of dual ultra-short echo time (UTE) images using a thresholding approach [11]. The uncorrected R2 map is calculated from the UTE images acquired at echo times TE_1 and TE_2. The R2 map is masked with an air mask derived from the first-echo image to generate the corrected R2 map. The corrected R2 map can be segmented into bone, soft-tissue, and air. *Keereman et al. 2010 J. Nucl. Med. 51(5) 812 doi:10.2967/jnumed.109.065425*

using an empirically determined threshold.

The fuzzy c-means (FCM) algorithm was implemented in several works. This unsupervised method generalises the k-means algorithm by allowing each data point to belong to multiple clusters with varying degrees of membership [14]. This is for example the case of Zaidi et al. [15], who applied the FCM algorithm on T1w spin-echo images to segment air, brain tissue, skull, nasal sinuses, and scalp. Some manual intervention of the operator was required to refine the segmentation of the skull. Later, Hsu et al. [16] applied it to segment a set of MR images (T1w, T2w, Dixon and UTE) into five tissue classes (fluid, fat, white matter, grey matter and bone). Su et al. [17] followed a similar idea but reduced the inputs to a single acquisition UTE-mDixon sequence. The three images derived from this sequence (fat, water and R2*) were used as inputs for an FCM algorithm aiming at identifying five clusters (air, brain, fat, fluid, and bone). They later extended the approach to thorax synthetic CT generation [18]. Instead of the UTE sequence, Khateri et al. [19] proposed to use a short echo time sequence, combined with a Dixon sequence, to segment the head in four tissue classes using FCM. Active learning-based classification was proposed in [20] to refine segmentations obtained with fuzzy clustering.

Other segmentation approaches have also been used. A knowledge-based segmentation approach consisting of three steps was proposed in [21]. First, tissues were segmented using a supervised neural network-based classification. The brain and extracerebral region were then separated based on anatomical knowledge: it is known that the brain soft-tissue is surrounded by cerebrospinal

fluid (CSF) which is in turn surrounded by the extracerebral region, while the extracerebral region is surrounded by the background region. Anatomical knowledge was finally used to segment the extracerebral region into the mastoid process, craniofacial cavities, bone, and soft-tissue, based for example on the fact that air-filled cavities are compact and connected by small junctions, while bone regions are narrow and elongated. Schulz et al. [22] based their 3-class (air, soft-tissue and lung) segmentation method on a T1w sequence. The body was first extracted from the background using slice-wise region growing with an automatically determined threshold, and another region growing was performed to segment the lungs. Instead of segmenting MR images, the use of non-attenuation corrected (NAC)-PET images was investigated in [23]. The 3-class segmentation consisted of segmenting the NAC-PET to derive a first attenuation map, using this map to correct the raw PET data for attenuation, and refining the segmentation using the newly reconstructed PET image. This process was repeated to first segment the body contour, then segment the lungs, and finally refine the lung segmentation. Instead of segmenting the skull in image space, Yang et al. [24] proposed a skull segmentation method for T1w MR images via a multiscale bilateral filtering processing of MRI sinogram data in the Radon domain. This segmentation method was combined with a multiscale FCM approach to classify the other tissues. In [25], air, bone and soft-tissue were segmented from brain UTE images using a multi-phase level-set approach. This active contour strategy allows segmenting images with more than two regions [26]. Finally, a 3D deep convolutional neural network (DeepMedic [27]) was trained in [28] to segment air, water, fat, and bone from T2w and Dixon images of the pelvis.

2.2 Intensity assignment approaches

Once the input image has been segmented, meaningful intensities must be assigned to each tissue class in order to obtain the synthetic image of interest.

2.2.1. Segmentation methods with bulk assignment

The simplest way to obtain a synthetic image from a segmented image is to assign predefined intensity values to each tissue class. This can be easily done when generating CT images as their voxels are displayed in terms of relative radiodensity expressed in Hounsfield unit (HU). For example, air has an attenuation of -1000 HU, fat between -120 and -90 HU, water of 0 HU, and cortical bone between 500 and 1900 HU. In their work illustrated in Figure 2, Jonsson et al. [4] assigned mass densities of 1.33 g/cm^3 to femoral bone, 1.025 g/cm^3 to soft-tissue and 0.001 g/cm^3 to air.

2.2.2. Segmentation methods with subject-specific assignment

The main drawback of assigning predefined values to the different tissue classes is that subject variability is not taken into account, which limits synthesis accuracy. This is particularly important in the MRI to CT image synthesis scenario for the bone region as it is known that several factors, such as age, can affect bone density [29, 30]. To overcome this limitation, several groups explored the possible existence of a mapping between the CT HU and MRI intensities, particularly R2* values in the bone region. If the ability of CT imaging to determine bone mineral content has been known for a long time [31], several studies showed that MR imaging could also provide some useful information. It was for example demonstrated using the UTE sequence that the water bound to the collagen in cortical bone (higher density) has a shorter spin-spin relaxation time T2 than the water present in the porous regions of cortical bone (lower density) [32]. As T2* includes T2 relaxation, it is expected that changes in R2* values (R2* = 1/T2*) would reflect changes in bone density.

Kapanen et al. [34] exploited in-phase images from a Dixon sequence to model the relation between MR intensity and HU within bone by fitting a second order polynomial. Pseudo CTs were generated by manually contouring the MR images, converting MR intensity values into HU within bone, and assigning to the other tissue classes a value of 0 HU.

Juttukonda et al. [35] acquired dual UTE and Dixon sequences from which they derived R2*, fat, water, and UTE_1 images used to segment bone, fat, soft-tissue, and air, respectively, based on simple thresholding. Predefined linear attenuation coefficients were then assigned to the air, fat and soft-tissues classes while tissues classified as bone were converted to HU using a regression model between the R2* values and HU. Several steps were necessary to obtain this model. First, the CT and R2* images of several subjects were aligned, and bone was segmented in both modalities using thresholds. To reduce noise, the R2* values were divided into bins. The mean R2* values and HU were then computed and plotted for each bin. Finally, a sigmoid model was fitted to the data.

Ladefoged et al. [33] also acquired and used UTE images to extract a continuous bone signal for each patient and map R2* values to HU. The model was however different as a third order polynomial was fitted instead of a sigmoid, see Figure 4. This could be explained by the lower threshold chosen for included bone and the different formula used to compute the R2* map. In addition to the R2* to HU mapping, they proposed to improve the attenuation map generation using regional masks to separately treat complex areas with mixed air and tissue. These regional masks, defined on an atlas, were transported into to subject's space and used, in combination with the R2* values, to assign predefined attenuation coefficients to the frontal sinus, nasal septa and ethmoidal sinus, mastoid process, and skull base.

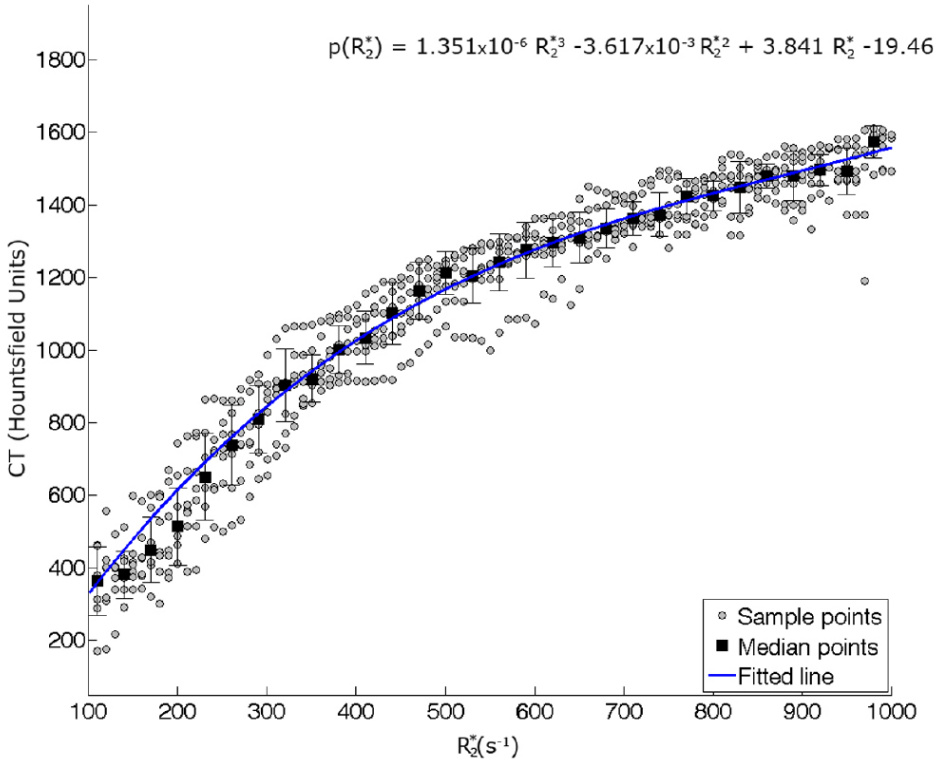

Figure 4: Illustration of how MR intensity values can be converted into CT Hounsfield units (HU) for subject-specific intensity assignment [33]. R2* versus HU scatter plot with sampled points are shown for each of the ten patients in grey. Every third median bin-value is shown with black squares. Standard deviation to the mean value is shown with black error bars. A 3rd order polynomial fit to the median points is shown with the blue line (goodness of fit $r^2 = 0.93$). *Ladefoged et al. 2015 Phys. Med. Biol. 60 8047 doi:10.1088/0031-9155/60/20/8047 © Institute of Physics and Engineering in Medicine. Reproduced by permission of IOP Publishing. All rights reserved.*

Other sequences have been exploited to convert MR intensities into CT HUs, mainly the zero echo-time (ZTE) sequence that allows capturing bone density variations [36, 37, 38, 39]. A linear regression was used to convert ZTE-normalized to HU values in the skull [38] while a two-segment piecewise linear model was used in pelvic bone regions [39]. Examples of brain pseudo CT images obtained with this approach are shown in Figure 5.

3. Registration-based image synthesis

In registration-based methods, an atlas is deformed to match the subject's anatomy using non-rigid registration. If we keep as use case MRI to CT image

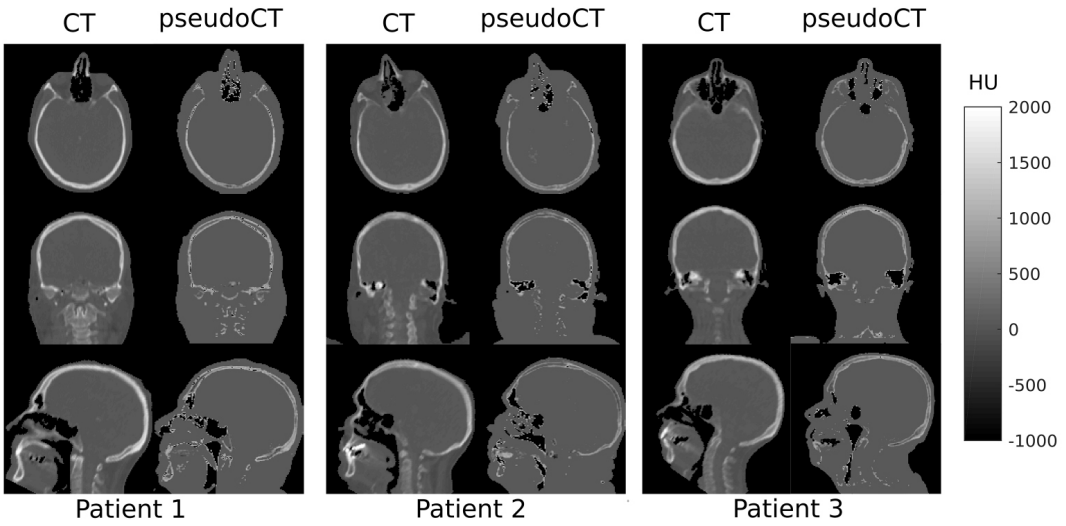

Figure 5: Three examples of CT images and ZTE-based pseudo-CTs generated using the segmentation algorithm and the linear relationship between normalized ZTE intensity and CT density in Hounsfield unit (HU) described in [38]. *Khalifé et al. 2017 Phys. Med. Biol. 62 7814 doi:10.1088/0031-9155/60/20/8047 © Institute of Physics and Engineering in Medicine. Reproduced by permission of IOP Publishing. All rights reserved.*

synthesis, the atlas can be composed of a single CT image, of a pair of MR and CT images, or of multiple pairs of MR and CT images, as illustrated in Figure 6. The principle was first introduced in 1993 by Miller et al [40].

3.1 Single-atlas registration approaches

3.1.1. Direct multimodal registration

When the atlas is composed of only one image of the target modality, a synthetic image is generated by directly registering the atlas to the source image of the subject of interest. The registration is thus multimodal. Schreibmann et al. [41] developed a multimodality optical flow deformable model mapping a representative CT template directly to the subject's MR image, thus generating a simulated CT image that matches the patient's anatomy. Multimodal inter-subject being the most challenging registration scenario, very few studies implemented a direct registration image synthesis approach.

3.1.2. Indirect unimodal registration

The majority of single-atlas registration approaches use an atlas composed of a pair of images: an image of the source contrast/modality and an image of the target contrast/modality. The source atlas image is registered to the

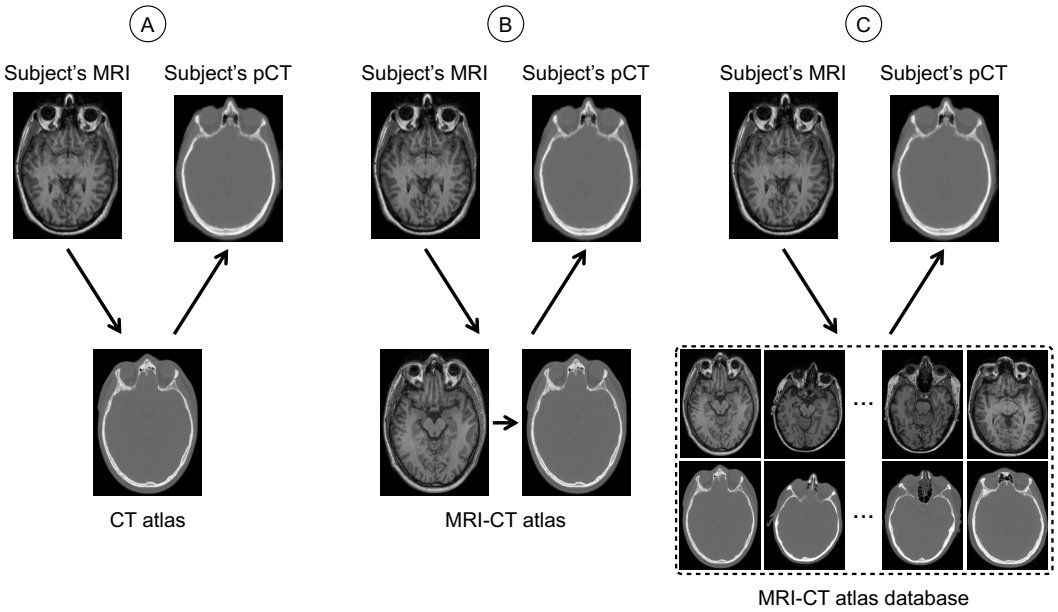

Figure 6: Registration-based approaches for image synthesis: direct multimodal (A) and indirect unimodal (B) single-atlas registration, and (C) multi-atlas registration. The atlas is composed of (A) a single CT image, (B) a pair of MRI and CT images, and (C) multiple pairs of MRI and CT images.

subject's source image and the resulting transformation is applied to the target atlas image to generate the subject's target image. The atlas can be obtained from a single individual but is most often obtained by averaging the images of multiple individuals. Long before the introduction of PET/MR scanners, researchers were already developing image synthesis approaches for attenuation correction. Huang et al. [42] did so in 1997 using a pair of transmission and emission scans as atlas. They proposed an inter-subject registration method to align the emission scan of the atlas to that of the target subject. The resulting transformation was then used to align the transmission scan of the atlas and generate a transmission scan for the subject under investigation.

Ten years later, Kops et al. [43] built a transmission-MRI atlas from the transmission and MR images of normal volunteers that were spatially normalised and averaged using the Statistical Parametric Mapping version 2 (SPM2)[1] software. To generate the subject's transmission image, the MRI atlas was registered to the subject's MR image and the same transformation was applied to the transmission atlas. With this method, it is possible to take into account morphological differences related to gender using female and male templates [44]. Downling et al. [45] proposed to generate a pseudo CT image by registering an MRI atlas, result of a groupwise registration, to the subject's

[1] http://www.fil.ion.ucl.ac.uk

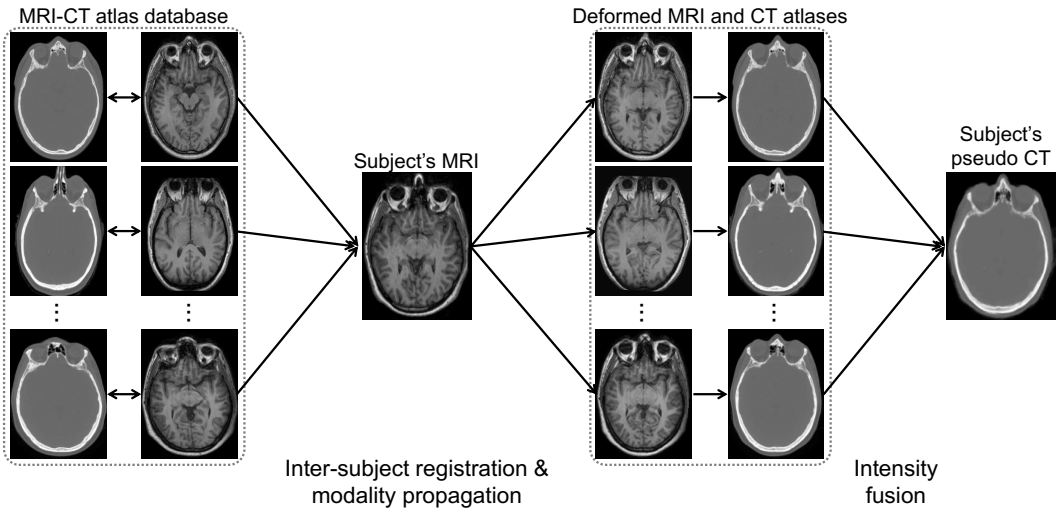

Figure 7: Multi-atlas registration approach to generate a pseudo CT from an MR image. All the MR images in the atlas database are registered to the subject's MR image. The CTs in the atlas database are then mapped using the same transformation to the subject's MR image. The subject's pseudo CT image is obtained by fusing the deformed atlas CT images.

MR image and applying the same transformation to a CT atlas aligned to the MRI atlas. Izquierdo-Garcia et al. [46] generated attenuation maps using the SPM8 software. The initial step of the method consisted of creating MRI and CT atlases. To do so, T1w MR images were first segmented into six tissue classes (grey matter, white matter, cerebrospinal fluid, bone, soft-tissue, and air) using SPM. The segmented images were then non-rigidly co-registered using Dartel [47] to form the MRI atlas. The same transformations were applied to the CT images, previously affinely aligned with the T1w images, and the CT atlas was created by averaging the co-registered CT images. To generate a pseudo CT, the MR image of the subject of interest is segmented into six tissue classes and non-rigidly registered to the MRI atlas. The associated CT atlas is finally mapped into the subject's space by applying the inverse transformation.

3.2 Multi-atlas registration approaches

The methods described in the previous section rely on a single atlas and strongly depend on the accuracy of the mapping between the atlas and subject spaces and on the representativeness of the atlas. A possible solution to improve the representativeness of the atlas and limit the consequences of mis-registrations is to use multiple atlases.

The multi-atlas methods reported below rely on a database of CT and MRI pairs. Each pair is created by registering the CT and MR images of a subject. To generate a pseudo CT from the subject's MR image, the MR images from

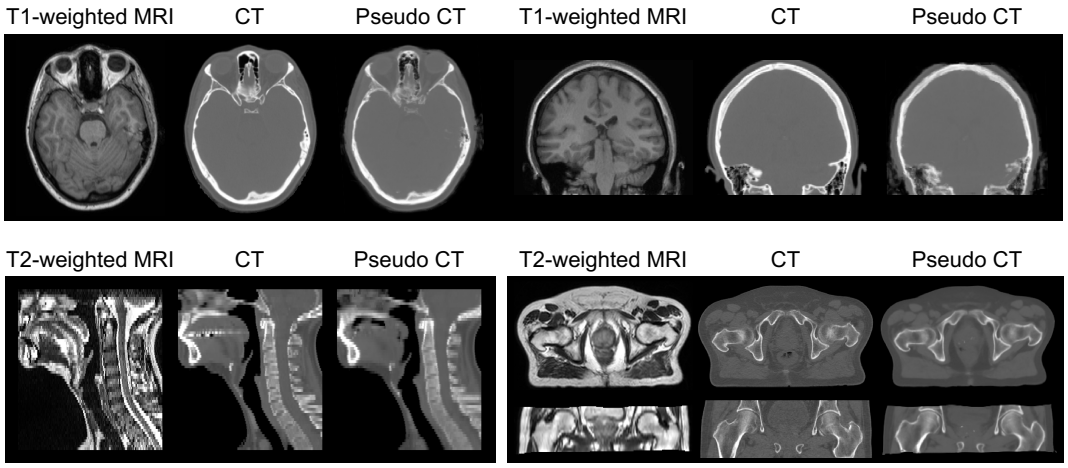

Figure 8: Examples of pseudo CT images obtained from MR images with a multi-atlas registration approach [6, 49, 51] in the brain (top), head & neck (bottom left) and pelvis (bottom right).

the database are non-rigidly registered to the subject's MRI. The CTs in the database are then mapped to the target subject using the transformation that maps the subject's corresponding MRI in the atlas database to the subject's MRI. A final step consists in fusing the deformed CT images. The approach is illustrated in Figure 7.

To fuse the deformed CTs, Sjolund et al. [48] proposed an iterative registration to the mean. The consistency of the deformed CTs was improved by iteratively forming their voxelwise mean, registering each deformed CT to the mean, and creating a new mean estimate. However, it appeared that better results were reached by directly taking the voxelwise median of the deformed CTs. Instead of computing the voxelwise median, Burgos et al. [49] obtained a pseudo CT by computing a weighted-average of the deformed CTs. The weights were derived from a local similarity measure computed between the MR image of the subject of interest and the MR images of the atlases. This image similarity measure reflects the morphological similarity, meaning that more weight is given to the atlases that are the most similar in terms of morphology to the subject of interest. This approach can generate pseudo CT images from a single [49] or multiple [50] MRI contrasts in the brain [49, 50], head & neck [6, 51] and pelvic [6] regions. See examples in Figure 8. A similar approach was implemented in [52]. Merida et al. [53] looked at the probability of a voxel in the subject space to belong to a certain tissue class. Three tissue classes (air, soft-tissue and bone) were defined by intensity thresholding the deformed CTs. The intensity value of the pseudo CT was determined by averaging for each voxel the CT intensities of the atlases belonging to the maximum probability class.

3.3 Combination of registration and regression approaches

To increase synthesis accuracy, several groups proposed to combine multi-atlas registration and regression approaches.

In the seminal work of Hofmann et al. [54], local information derived from a supervised learning technique and global information obtained from multi-atlas registration were combined to predict a pseudo CT image: multi-atlas registration was used as prior knowledge for a Gaussian process regression. The global step of the method consisted of non-rigidly registering the MR images from the training dataset to the subject's MR image and applying the same transformations to the corresponding CT images in the training dataset. The local step aimed at determining a mapping between MR image patches centred at a voxel of interest and the real CT HU values using Gaussian process regression. Training pairs comprising the position of the voxel in the subject coordinate system and the patch surrounding it were extracted from the deformed images in the training dataset. Prior knowledge from the atlas registration was included by setting the mean function of the Gaussian process to the average value of the registered CT images. For an unseen patch, Gaussian process regression returned a Gaussian-distributed predictive distribution for the mapping of the MR patches to the CT HU. Finally, to predict a pseudo CT image for a new subject, for each voxel of the MR image a surrounding patch was extracted and the mean of the Gaussian-distributed predictive distribution was defined as the estimated CT value. The method was also adapted to whole-body attenuation correction [55].

A similar approach combining intensity and geometry information into a unifying probabilistic Bayesian framework was later proposed [56]. The method implemented in [57] relies on a database of co-registered T1w MR images, CT images and air masks segmented from the CT images using k-means clustering. Pseudo CT generation required three steps. First, each atlas was non-rigidly registered to the subject's MR image. A probabilistic air mask was then computed as the percentage of the aligned CT atlases that labelled a voxel as air, and refined using a hidden Markov random field segmentation on the T1w MR image. Each voxel labelled as air was assigned the mean value of the atlas CTs belonging to the air mask. For the rest of the tissues, small neighbourhoods centred around each voxel were defined in the target. Patches of the same size were defined in the atlases in the vicinity of the central voxel. Sparse regression was then used to select the most similar patches, in terms of intensity, among all the atlas patches within the search window. Finally, the sparse coefficients were applied to combine the atlas CTs and generate the pseudo CT. More details on the use of dictionary learning for image synthesis can be found in Chapter 5.

4. Hybrid approaches combining segmentation and registration

The methods described in this section combine both image segmentation and registration to generate synthetic images.

Bezrukov et al. [58] proposed a method combining segmentation, multi-atlas registration and supervised learning techniques, which relied on the subject's Dixon images and on an atlas database. Each atlas comprised a 5-tissue class segmentation (outer air, lung, fat tissue, non-fat tissue, and fat/non-fat tissue mix), a map of potential artefact locations extracted from regions with low MR intensity and differentiated into air-filled regions not part of the lungs and soft-tissue regions, a CT image, and a bone location map. After segmentation of the subject's MR image into five tissue classes, the segmented MR images from the atlas database were registered to the subject's image and the resulting transformations were applied to the images forming the atlases. A subject-specific map of potential artefact locations was created by averaging the atlas artefact maps. This map was used to classify the low MRI intensity regions as inside air or soft-tissue masked by artefacts. Predefined linear attenuation coefficients were assigned to the segmented regions of the MR image to create an intermediate attenuation map. For the prediction of bone tissue, a map of potential bone locations was created from the atlas CT images by combining the individual bone location maps. This map determined the areas where Gaussian process regression was applied. For each voxel within these areas, a pseudo CT value was computed from the CT atlases and converted to linear attenuation coefficients using a piecewise linear transformation. The final attenuation map was created by augmenting the intermediate attenuation map with the predicted bone linear attenuation coefficients.

Combining the segmentation of an MR image and the use of a CT image database, Marshall et al. [59] proposed a method where the subject's MR image was compared to an atlas database of CT images using a set of 19 similarity metrics such as gender, age, and body, lung and bone geometries. The most similar CT image was selected and non-rigidly aligned to the subject's MR image. Bones from the registered CT image were then added to the MR image previously segmented into four tissue classes (air, lung, fat and lean tissue).

Exploiting multiple MRI sequences, Anazodo et al. [60] proposed to overlay a bone mask to the attenuation map obtained from the segmentation of Dixon images [8]. The bone mask was created by segmenting a T1w magnetisation-prepared rapid gradient-echo image using the *New Segment* function from SPM8 [61]. SPM has also been used in [62].

The method implemented by Paulus et al. [63], illustrated in Figure 9, was based on a regular 4-class segmentation from a Dixon sequence and atlas-based bone segmentation algorithm. The atlas was composed of pairs of pre-aligned

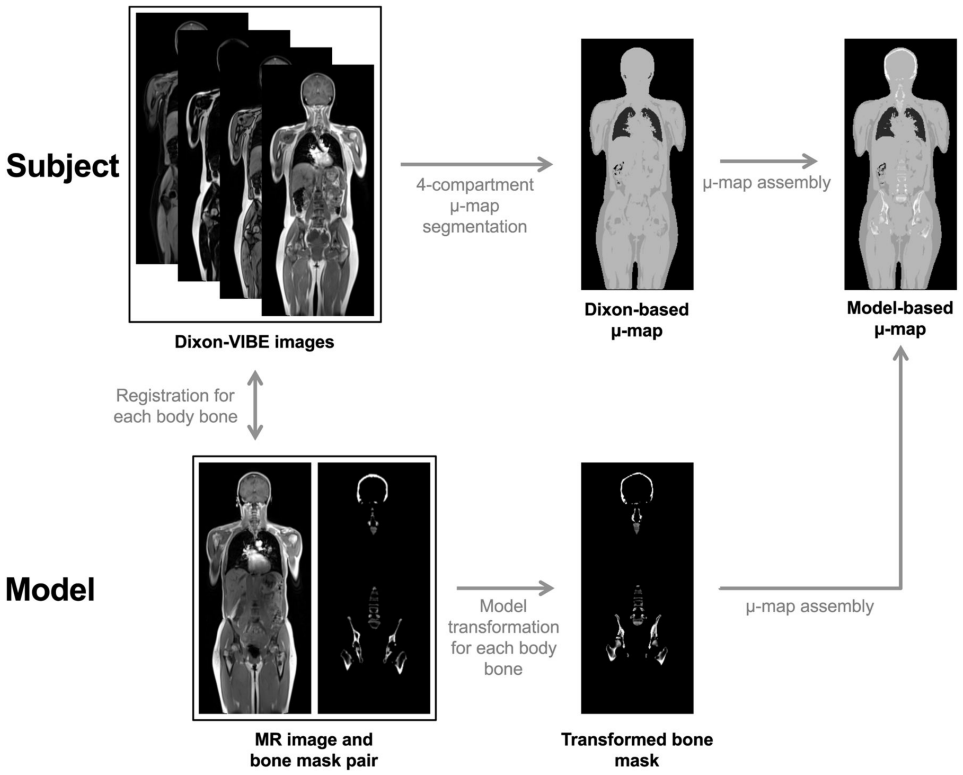

Figure 9: Schematic drawing of the hybrid segmentation/registration-based approach for considering bone in whole-body PET/MR attenuation correction [63]. The subject-specific attenuation map (μ-map) is generated by first segmenting the subject's Dixon images into four classes (air, lung, soft-tissue and fat). The bone class is then added by registering the MR model to the subject for each bone individually and applying the same transformation to the bone mask. *Paulus et al. 2015 J. Nucl. Med. 56 1061 doi:10.2967/jnumed.115.156000*

MR image and bone mask (containing bone densities) for each major bone in the body, including left and right upper femur, left and right hip, spine, and skull. To generate a subject-specific attenuation map, the subject's Dixon images were first segmented into four classes (air, lung, soft-tissue and fat). The bone class was then added by registering the MR model to the subject for each bone individually and applying the same transformation to the bone mask. The method was then validated in the brain region [64].

In their work, Arabi et al. [65] combined multi-atlas segmentation and synthesis with the aim to improve the synthesis of CT images from MRI in the bone region. Their framework consisted of two steps. In the first one, bone was segmented using multi-atlas segmentation. In the second one, a pseudo CT was generated using a multi-atlas approach, the atlases being fused based on the resemblance of both the bone map obtained at the first step and the morphological similarity to the MR image of the subject being analysed.

5. Future directions and research challenges

In this chapter, we covered image synthesis approaches that rely on well-established image processing techniques: segmentation and registration. The vast majority of these approaches have been applied to the synthesis of CT from MR images. This can be explained by two reasons. First, these image synthesis approaches were developed to answer particular needs: that of accurate electron density estimation when only MR images are available, which occurs in the context of both PET/MR attenuation correction (see Chapter 19) and MRI-only RTP (see Chapter 20). The second reason is that their accuracy appears limited on other tasks, which is why they have been supplanted by better performing methods.

The development of MR to CT image synthesis approaches followed the development of new technologies. Regarding attenuation correction, even though first attempts of synthesising attenuation maps date back to the 1990s [42], many works have accompanied the release of PET/MR scanners (2010 for Philips and Siemens Healthineers, 2011 for GE Healthcare). Prototypes of MR-Linac date back to the same period [66]. These technological developments led to new problems, namely the fact that MR image intensities do not directly provide information about the tissue attenuation properties, to which image synthesis was proposed as a solution.

Segmentation-based methods essentially rely on the subject's MR images. This explains why specific sequences such as the Dixon, UTE or ZTE, often only acquired for the purpose of image synthesis, have been employed. Various segmentation strategies have been implemented: manual segmentation, mainly in the context of RTP and/or as proof of concept, and a large range of automatic methods that include mainly intensity thresholding and fuzzy c-means. Initially, once segmented, predefined values were often assigned to each tissue class, but subject-specific assignments have shown their superiority, especially in bone regions. A limitation of segmentation methods is the difficulty in delineating tissues in regions with air/tissue and air/bone interfaces. Another one is their susceptibility to MR image artefacts.

Registration-based methods rely on both the subject's MR images and on an atlas or database of atlases. The first methods developed relied on a single atlas to generate a subject-specific attenuation map. Their accuracy was limited as a single template can hardly be representative of all the potential patients, even if they do not present morphological abnormalities. These methods also strongly depend on the accuracy of the registration used to map the atlas to the target subject. A solution to both improve the representativeness of the atlas and reduce the impact of registration inaccuracies has been to use a database of atlases. However, this comes with the price of having to run multiple, time-consuming, non-rigid registrations. Another limitation is

the limited ability of these methods to handle anatomical abnormalities (e.g. unusual bone density).

The second reason that can explain the use of segmentation and registration-based approaches to only MR to CT image synthesis is that their accuracy appears limited on other tasks. Jog et al. [67] for example compared a multi-atlas registration approach with their random forest regression method for the synthesis of T2w from T1w MR images and of FLAIR from T1-, T2-, and proton density-weighted MR images, and observed that the multi-atlas registration approach led to blurrier images from which lesions were barely visible. Multi-atlas registration has nonetheless successfully been used to generate pseudo-healthy PET images from T1w MR images [68, 69]. Many techniques have now supplanted segmentation and registration-based approaches, starting with patch-based methods that do not require non-rigid alignment between the training and target subjects (more in Chapter 5) until the nowadays highly predominant deep learning approaches (more in Chapters 6, 7 and 8).

Interested readers can find further information in several reviews and comparison articles. In the context of RTP, approaches that exist to generate synthetic CT images have been reviewed for example in [70, 71, 72] while their performance has been compared in [73, 74]. Several reviews have been published over the years regarding image synthesis for attenuation correction [75, 76, 77, 78, 79, 80], and Ladefoged et al. [81] published a multi-centre study aiming at evaluating the performance of various attenuation correction methods, including five segmentation-based [8, 10, 12, 33, 35], three atlas-based [46, 49, 53] and two hybrid approaches combining segmentation and use of an atlas [60, 64].

6. Summary

Even though medical image synthesis can be used to improve subsequent image processing techniques such as segmentation or registration, in this chapter we saw how segmentation and registration could themselves be used for image synthesis. Segmentation-based approaches consist in segmenting the source image, either manually or automatically, and assigning intensity values to the different tissue classes obtained, using bulk or subject-specific assignment, to generate the desired image. Registration-based methods consist in deforming an atlas, composed of a single image, a pair of images or multiple pairs, to match the subject's anatomy using non-rigid registration. Most segmentation- and registration-based image synthesis approaches have been used to synthesise CT from MR images in the context of PET(/MR) attenuation correction and MRI-only radiotherapy treatment planning. Even though these techniques helped answer concrete needs, they have now been supplanted by deep learning methods.

Acknowledgments

The research leading to these results has received funding from the French government under management of Agence Nationale de la Recherche as part of the "Investissements d'avenir" program, ref. ANR-19-P3IA-0001 (PRAIRIE 3IA Institute) and ANR-10-IAIHU-0006 (Agence Nationale de la Recherche - 10-IA Institut Hospitalo-Universitaire-6).

References

[1] van de Kraats EB, Penney GP, van Walsum T, Niessen WJ (2005) Multispectral MR to X-ray registration of vertebral bodies by generating CT-like data. In: Duncan JS, Gerig G (eds) Medical Image Computing and Computer-Assisted Intervention – MICCAI 2005, Springer, Lecture Notes in Computer Science, pp 911–918

[2] Roy S, Carass A, Shiee N, Pham DL, Prince JL (2010) MR contrast synthesis for lesion segmentation. In: 2010 IEEE International Symposium on Biomedical Imaging: From Nano to Macro, pp 932–935

[3] Prince JL, Carass A, Zhao C, Dewey BE, Roy S, Pham DL (2020) Image synthesis and superresolution in nedical imaging. In: Zhou SK, Rueckert D, Fichtinger G (eds) Handbook of Medical Image Computing and Computer Assisted Intervention, Academic Press, pp 1–24

[4] Jonsson JH, Karlsson MG, Karlsson M, Nyholm T (2010) Treatment planning using MRI data: An analysis of the dose calculation accuracy for different treatment regions. Radiation Oncology 5:62

[5] Korhonen J, Kapanen M, Keyriläinen J, Seppälä T, Tenhunen M (2014) A dual model HU conversion from MRI intensity values within and outside of bone segment for MRI-based radiotherapy treatment planning of prostate cancer. Medical Physics 41(1):011704

[6] Guerreiro F, Burgos N, Dunlop A, Wong K, Petkar I, Nutting C, Harrington K, Bhide S, Newbold K, Dearnaley D, deSouza NM, Morgan VA, McClelland J, Nill S, Cardoso MJ, Ourselin S, Oelfke U, Knopf AC (2017) Evaluation of a multi-atlas CT synthesis approach for MRI-only radiotherapy treatment planning. Physica Medica 35:7–17

[7] Le Goff-Rougetet R, Frouin V, Mangin JF, Bendriem B (1994) Segmented MR images for brain attenuation correction in PET. In: Medical Imaging 1994, pp 725–736

[8] Martinez-Möller A, Souvatzoglou M, Delso G, Bundschuh RA, Chefd'hotel C, Ziegler SI, Navab N, Schwaiger M, Nekolla SG (2009) Tissue classification as a

potential approach for attenuation correction in whole-body PET/MRI: Evaluation with PET/CT data. Journal of Nuclear Medicine 50(4):520–6

[9] Dixon WT (1984) Simple proton spectroscopic imaging. Radiology 153(1):189–194

[10] Catana C, van der Kouwe A, Benner T, Michel CJ, Hamm M, Fenchel M, Fischl B, Rosen B, Schmand M, Sorensen aG (2010) Toward implementing an MRI-based PET attenuation-correction method for neurologic studies on the MR-PET brain prototype. Journal of Nuclear Medicine 51(9):1431–8

[11] Keereman V, Fierens Y, Broux T, De Deene Y, Lonneux M, Vandenberghe S (2010) MRI-based attenuation correction for PET/MRI using ultrashort echo time sequences. Journal of Nuclear Medicine 51(5):812–8

[12] Cabello J, Lukas M, Förster S, Pyka T, Nekolla SG, Ziegler SI (2015) MR-Based attenuation correction using ultrashort-echo-time pulse sequences in dementia patients. Journal of Nuclear Medicine 56(3):423–429

[13] Berker Y, Franke J, Salomon A, Palmowski M, Donker HCW, Temur Y, Mottaghy FM, Kuhl C, Izquierdo-Garcia D, Fayad ZA, Kiessling F, Schulz V (2012) MRI-based attenuation correction for hybrid PET/MRI systems: A 4-class tissue segmentation technique using a combined ultrashort-echo-time/Dixon MRI sequence. Journal of Nuclear Medicine 53(5):796–804

[14] Bezdek JC (1981) Pattern Recognition with Fuzzy Objective Function Algorithms. Advanced Applications in Pattern Recognition, Springer US

[15] Zaidi H, Montandon ML, Slosman DO (2003) Magnetic resonance imaging-guided attenuation and scatter corrections in three-dimensional brain positron emission tomography. Medical Physics 30(5):937–948

[16] Hsu SH, Cao Y, Huang K, Feng M, Balter JM (2013) Investigation of a method for generating synthetic CT models from MRI scans of the head and neck for radiation therapy. Physics in Medicine and Biology 58(23):8419

[17] Su KH, Hu L, Stehning C, Helle M, Qian P, Thompson CL, Pereira GC, Jordan DW, Herrmann KA, Traughber M, Muzic RF, Traughber BJ (2015) Generation of brain pseudo-CTs using an undersampled, single-acquisition UTE-mDixon pulse sequence and unsupervised clustering. Medical Physics 42(8):4974–4986

[18] Su KH, Friel HT, Kuo JW, Helo RA, Baydoun A, Stehning C, Crisan AN, Traughber MS, Devaraj A, Jordan DW, Qian P, Leisser A, Ellis RJ, Herrmann KA, Avril N, Traughber BJ, Muzic RF (2019) UTE-mDixon-based thorax synthetic CT generation. Medical Physics 46(8):3520–3531

[19] Khateri P, Rad HS, Jafari AH, Kazerooni AF, Akbarzadeh A, Moghadam MS, Aryan A, Ghafarian P, Ay MR (2015) Generation of a four-class attenuation

map for MRI-based attenuation correction of PET data in the head area using a novel combination of STE/Dixon-MRI and FCM clustering. Molecular Imaging and Biology 17(6):884–892

[20] Qian P, Chen Y, Kuo J, Zhang Y, Jiang Y, Zhao K, Helo RA, Friel H, Baydoun A, Zhou F, Heo JU, Avril N, Herrmann K, Ellis R, Traughber B, Jones RS, Wang S, Su K, Muzic RF (2020) mDixon-based synthetic CT generation for PET attenuation correction on abdomen and pelvis jointly using transfer fuzzy clustering and active learning-based classification. IEEE Transactions on Medical Imaging 39(4):1–1

[21] Wagenknecht G, Kops ER, Tellmann L, Herzog H (2009) Knowledge-based segmentation of attenuation-relevant regions of the head in T1-weighted MR images for attenuation correction in MR/PET systems. In: Nuclear Science Symposium Conference Record, 2009. NSS'09. IEEE, pp 3338–3343

[22] Schulz V, Torres-Espallardo I, Renisch S, Hu Z, Ojha N, Börnert P, Perkuhn M, Niendorf T, Schäfer WM, Brockmann H, Krohn T, Buhl A, Günther RW, Mottaghy FM, Krombach GA (2011) Automatic, three-segment, MR-based attenuation correction for whole-body PET/MR data. European Journal of Nuclear Medicine and Molecular Imaging 38(1):138–152

[23] Chang T, Diab RH, Clark Jr JW, Mawlawi OR (2013) Investigating the use of nonattenuation corrected PET images for the attenuation correction of PET data. Medical Physics 40(8):082508

[24] Yang X, Fei B (2013) Multiscale segmentation of the skull in MR images for MRI-based attenuation correction of combined MR/PET. Journal of the American Medical Informatics Association 20(6):1037–1045

[25] An HJ, Seo S, Kang H, Choi H, Cheon GJ, Kim HJ, Lee DS, Song IC, Kim YK, Lee JS (2016) MRI-based attenuation correction for PET/MRI using multiphase level-set method. Journal of Nuclear Medicine 57(4):587–593

[26] Vese LA, Chan TF (2002) A multiphase level set framework for image segmentation using the Mumford and Shah model. International Journal of Computer Vision 50(3):271–293

[27] Kamnitsas K, Ledig C, Newcombe V, Simpson J, Kane A, Menon D, Rueckert D, Glocker B (2017) Efficient multi-scale 3D CNN with fully connected CRF for accurate brain lesion segmentation. Medical Image Analysis 36:61–78

[28] Bradshaw TJ, Zhao G, Jang H, Liu F, McMillan AB (2018) Feasibility of deep learning-based PET/MR attenuation correction in the pelvis using only diagnostic MR images. Tomography 4(3):138–147

[29] Fehily AM, Coles RJ, Evans WD, Elwood PC (1992) Factors affecting bone density in young adults. The American Journal of Clinical Nutrition 56(3):579–586

[30] Schulte-Geers C, Obert M, Schilling R, Harth S, Traupe H, Gizewski E, Verhoff M (2011) Age and gender-dependent bone density changes of the human skull disclosed by high-resolution flat-panel computed tomography. International Journal of Legal Medicine 125(3):417–425

[31] Reich NE, Seidelmann FE, Tubbs R, Mac Intyre WJ, Meaney T, Alfidi R, Pepe R (1976) Determination of bone mineral content using CT scanning. American Journal of Roentgenology 127(4):593–594

[32] Horch RA, Nyman JS, Gochberg DF, Dortch RD, Does MD (2010) Characterization of ^{1}H NMR signal in human cortical bone for magnetic resonance imaging. Magnetic Resonance in Medicine 64(3):680–687

[33] Ladefoged CN, Benoit D, Law I, Holm S, Kjær A, Højgaard L, Hansen AE, Andersen FL (2015) Region specific optimization of continuous linear attenuation coefficients based on UTE (RESOLUTE): Application to PET/MR brain imaging. Physics in Medicine and Biology 60(20):8047

[34] Kapanen M, Tenhunen M (2013) T1/T2*-weighted MRI provides clinically relevant pseudo-CT density data for the pelvic bones in MRI-only based radiotherapy treatment planning. Acta Oncologica 52(3):612–618

[35] Juttukonda MR, Mersereau BG, Chen Y, Su Y, Rubin BG, Benzinger TL, Lalush DS, An H (2015) MR-based attenuation correction for PET/MRI neurological studies with continuous-valued attenuation coefficients for bone through a conversion from R2* to CT-Hounsfield units. NeuroImage 112:160–168

[36] Wiesinger F, Sacolick LI, Menini A, Kaushik SS, Ahn S, Veit-Haibach P, Delso G, Shanbhag DD (2016) Zero TE MR bone imaging in the head. Magnetic Resonance in Medicine 75(1):107–114

[37] Huang C, Ouyang J, Reese T, Wu Y, El Fakhri G, Ackerman J (2015) Continuous MR bone density measurement using water-and fat-suppressed projection imaging (WASPI) for PET attenuation correction in PET-MR. Physics in Medicine and Biology 60(20):N369

[38] Khalifé M, Fernandez B, Jaubert O, Soussan M, Brulon V, Buvat I, Claude Comtat (2017) Subject-specific bone attenuation correction for brain PET/MR: Can ZTE-MRI substitute CT scan accurately? Physics in Medicine & Biology 62(19):7814

[39] Leynes AP, Yang J, Shanbhag DD, Kaushik SS, Seo Y, Hope TA, Wiesinger F, Larson PEZ (2017) Hybrid ZTE/Dixon MR-based attenuation correction for quantitative uptake estimation of pelvic lesions in PET/MRI. Medical Physics 44(3):902–913

[40] Miller MI, Christensen GE, Amit Y, Grenander U (1993) Mathematical textbook of deformable neuroanatomies. Proceedings of the National Academy of Sciences 90(24):11944–11948

[41] Schreibmann E, Nye JA, Schuster DM, Martin DR, Votaw J, Fox T (2010) MR-based attenuation correction for hybrid PET-MR brain imaging systems using deformable image registration. Medical Physics 37(5):2101

[42] Huang CL, Chang WT, Wu LC, Wang JK (1997) Three-dimensional PET emission scan registration and transmission scan synthesis. IEEE Transactions on Medical Imaging 16(5):542–561

[43] Kops ER, Herzog H (2007) Alternative methods for attenuation correction for PET images in MR-PET scanners. In: Nuclear Science Symposium Conference Record, 2007. NSS'07. IEEE, vol 6, pp 4327–4330

[44] Kops ER, Herzog H (2008) Template based attenuation correction for PET in MR-PET scanners. In: Nuclear Science Symposium Conference Record, 2008. NSS'08. IEEE, pp 3786–3789

[45] Dowling JA, Lambert J, Parker J, Salvado O, Fripp J, Capp A, Wratten C, Denham JW, Greer PB (2012) An atlas-based electron density mapping method for magnetic resonance imaging (MRI)-alone treatment planning and adaptive MRI-based prostate radiation therapy. International Journal of Radiation Oncology · Biology · Physics 83(1):e5–e11

[46] Izquierdo-Garcia D, Hansen AE, Förster S, Benoit D, Schachoff S, Fürst S, Chen KT, Chonde DB, Catana C (2014) An SPM8-based approach for attenuation correction combining segmentation and nonrigid template formation: Application to simultaneous PET/MR brain imaging. Journal of Nuclear Medicine 55(11):1825–1830

[47] Ashburner J (2007) A fast diffeomorphic image registration algorithm. NeuroImage 38(1):95–113

[48] Sjölund J, Forsberg D, Andersson M, Knutsson H (2015) Generating patient specific pseudo-CT of the head from MR using atlas-based regression. Physics in Medicine and Biology 60(2):825

[49] Burgos N, Cardoso MJ, Thielemans K, Modat M, Pedemonte S, Dickson J, Barnes A, Ahmed R, Mahoney CJ, Schott JM, Duncan JS, Atkinson D, Arridge SR, Hutton BF, Ourselin S (2014) Attenuation correction synthesis for hybrid PET-MR scanners: Application to brain studies. Medical Imaging, IEEE Transactions on 33(12):2332–2341

[50] Burgos N, Cardoso MJ, Thielemans K, Modat M, Dickson J, Schott JM, Atkinson D, Arridge SR, Hutton BF, Ourselin S (2015) Multi-contrast attenuation map synthesis for PET/MR scanners: Assessment on FDG and Florbetapir PET tracers. European Journal of Nuclear Medicine and Molecular Imaging 42(9):1447–1458

[51] Burgos N, Cardoso MJ, Guerreiro F, Veiga C, Modat M, McClelland J, Knopf A, Punwani S, Atkinson D, Arridge SR, Hutton BF, Ourselin S (2015) Robust CT synthesis for radiotherapy planning: Application to the head & neck region. In: Medical Image Computing and Computer-Assisted Intervention – MICCAI 2015, pp 476–484

[52] Dowling JA, Sun J, Pichler P, Rivest-Hénault D, Ghose S, Richardson H, Wratten C, Martin J, Arm J, Best L, Chandra SS, Fripp J, Menk FW, Greer PB (2015) Automatic substitute computed tomography generation and contouring for magnetic resonance imaging (MRI)-alone external beam radiation therapy from standard MRI sequences. International Journal of Radiation Oncology · Biology · Physics 93(5):1144–1153

[53] Mérida I, Reilhac A, Redouté J, Heckemann RA, Costes N, Hammers A (2017) Multi-atlas attenuation correction supports full quantification of static and dynamic brain PET data in PET-MR. Physics in Medicine & Biology 62(7):2834

[54] Hofmann M, Steinke F, Scheel V, Charpiat G, Farquhar J, Aschoff P, Brady M, Schölkopf B, Pichler BJ (2008) MRI-based attenuation correction for PET/MRI: A novel approach combining pattern recognition and atlas registration. Journal of Nuclear Medicine 49(11):1875–83

[55] Hofmann M, Bezrukov I, Mantlik F, Aschoff P, Steinke F, Beyer T, Pichler BJ, Schölkopf B (2011) MRI-based attenuation correction for whole-body PET/MRI: Quantitative evaluation of segmentation-and atlas-based methods. Journal of Nuclear Medicine 52(9):1392–1399

[56] Gudur MSR, Hara W, Le QT, Wang L, Xing L, Li R (2014) A unifying probabilistic Bayesian approach to derive electron density from MRI for radiation therapy treatment planning. Physics in Medicine and Biology 59(21):6595

[57] Chen Y, Juttukonda M, Su Y, Benzinger T, Rubin BG, Lee YZ, Lin W, Shen D, Lalush D, An H (2015) Probabilistic air segmentation and sparse regression estimated pseudo CT for PET/MR attenuation correction. Radiology 275(2):562–569

[58] Bezrukov I, Schmidt H, Mantlik F, Schwenzer N, Brendle C, Schölkopf B, Pichler BJ (2013) MR-based attenuation correction methods for improved PET quantification in lesions within bone and susceptibility artifact regions. Journal of Nuclear Medicine 54(10):1768–1774

[59] Marshall HR, Patrick J, Laidley D, Prato FS, Butler J, Théberge J, Thompson RT, Stodilka RZ (2013) Description and assessment of a registration-based approach to include bones for attenuation correction of whole-body PET/MRI. Medical Physics 40(8):082509

[60] Anazodo UC, Thiessen JD, Ssali T, Mandel J, Günther M, Butler J, Pavlosky W, Prato FS, Thompson RT, Lawrence KSS (2015) Feasibility of simultaneous

whole-brain imaging on an integrated PET-MRI system using an enhanced 2-point Dixon attenuation correction method. Frontiers in Neuroscience 8:434

[61] Ashburner J, Friston KJ (2005) Unified segmentation. NeuroImage 26(3):839–851

[62] Teuho J, Linden J, Johansson J, Tuisku J, Tuokkola T, Teräs M (2016) Tissue probability-based attenuation correction for brain PET/MR by using SPM8. IEEE Transactions on Nuclear Science 63(5):2452–2463

[63] Paulus DH, Quick HH, Geppert C, Fenchel M, Zhan Y, Hermosillo G, Faul D, Fernando B, Friedman K, Koesters T (2015) Whole-body PET/MR imaging: Quantitative evaluation of a novel model-based MR attenuation correction method including bone. Journal of Nuclear Medicine 56(7):1061–1066

[64] Koesters T, Friedman KP, Fenchel M, Zhan Y, Hermosillo G, Babb J, Jelescu IO, Faul D, Boada FE, Shepherd TM (2016) Dixon sequence with superimposed model-based bone compartment provides highly accurate PET/MR attenuation correction of the brain. Journal of Nuclear Medicine 57(6):918–924

[65] Arabi H, Koutsouvelis N, Rouzaud M, Miralbell R, Zaidi H (2016) Atlas-guided generation of pseudo-ct images for mri-only and hybrid pet–mri-guided radiotherapy treatment planning. Physics in Medicine & Biology 61(17):6531

[66] Lagendijk JJ, Raaymakers BW, Raaijmakers AJ, Overweg J, Brown KJ, Kerkhof EM, van der Put RW, Hårdemark B, van Vulpen M, van der Heide UA (2008) MRI/linac integration. Radiotherapy and Oncology 86(1):25–29

[67] Jog A, Carass A, Roy S, Pham DL, Prince JL (2017) Random forest regression for magnetic resonance image synthesis. Medical Image Analysis 35:475–488

[68] Burgos N, Cardoso MJ, Mendelson A, Schott JM, Atkinson D, Arridge SR, Hutton BF, Ourselin S (2015) Subject-specific models for the analysis of pathological FDG PET data. In: Medical Image Computing and Computer-Assisted Intervention – MICCAI 2015, pp 651–658

[69] Burgos N, Cardoso MJ, Samper-González J, Habert MO, Durrleman S, Ourselin S, Colliot O (2021) Anomaly detection for the individual analysis of brain PET images. Journal of Medical Imaging 8(2):024003

[70] Edmund JM, Nyholm T (2017) A review of substitute CT generation for MRI-only radiation therapy. Radiation Oncology 12:28

[71] Johnstone E, Wyatt JJ, Henry AM, Short SC, Sebag-Montefiore D, Murray L, Kelly CG, McCallum HM, Speight R (2018) Systematic review of synthetic computed tomography generation methodologies for use in magnetic resonance imaging-only radiation therapy. International Journal of Radiation Oncology · Biology · Physics 100(1):199–217

[72] Dowling JA, Korhonen J (2019) MR-only methodology. In: Liney G, van der Heide U (eds) MRI for Radiotherapy: Planning, Delivery, and Response Assessment, Springer, pp 131–151

[73] Arabi H, Dowling JA, Burgos N, Han X, Greer PB, Koutsouvelis N, Zaidi H (2018) Comparative study of algorithms for synthetic CT generation from MRI: consequences for MRI-guided radiation planning in the pelvic region. Medical Physics 45(11):5218–5233

[74] Largent A, Barateau A, Nunes JC, Lafond C, Greer PB, Dowling JA, Saint-Jalmes H, Acosta O, de Crevoisier R (2019) Pseudo-CT generation for MRI-only radiation therapy treatment planning: comparison among patch-based, atlas-based, and bulk density methods. International Journal of Radiation Oncology · Biology · Physics 103(2):479–490

[75] Hofmann M, Pichler B, Schölkopf B, Beyer T (2009) Towards quantitative PET/MRI: A review of MR-based attenuation correction techniques. European Journal of Nuclear Medicine and Molecular Imaging 36(S1):93–104

[76] Bezrukov I, Mantlik F, Schmidt H, Schölkopf B, Pichler BJ (2013) MR-based PET attenuation correction for PET/MR imaging. Seminars in Nuclear Medicine 43(1):45–59

[77] Keereman V, Mollet P, Berker Y, Schulz V, Vandenberghe S (2013) Challenges and current methods for attenuation correction in PET/MR. Magnetic Resonance Materials in Physics, Biology and Medicine 26(1):81–98

[78] Wagenknecht G, Kaiser HJ, Mottaghy FM, Herzog H (2013) MRI for attenuation correction in PET: Methods and challenges. Magnetic Resonance Materials in Physics, Biology and Medicine 26(1):99–113

[79] Izquierdo-Garcia D, Catana C (2016) MR imaging-guided attenuation correction of PET data in PET/MR imaging. PET Clinics 11(2):129–149

[80] Mehranian A, Arabi H, Zaidi H (2016) Vision 20/20: magnetic resonance imaging-guided attenuation correction in PET/MRI: Challenges, solutions, and opportunities. Medical Physics 43(3):1130–1155

[81] Ladefoged CN, Law I, Anazodo U, St Lawrence K, Izquierdo-Garcia D, Catana C, Burgos N, Cardoso MJ, Ourselin S, Hutton B, Mérida I, Costes N, Hammers A, Benoit D, Holm S, Juttukonda M, An H, Cabello J, Lukas M, Nekolla S, Ziegler S, Fenchel M, Jakoby B, Casey ME, Benzinger T, Højgaard L, Hansen AE, Andersen FL (2017) A multi-centre evaluation of eleven clinically feasible brain pet/mri attenuation correction techniques using a large cohort of patients. NeuroImage 147(Supplement C):346–359